Drop Formation in Non-Newtonian Jets at Low Reynolds Numbers

V. Dravid[1]
P. B. Loke
C. M. Corvalan[2]
P. E. Sojka[2,3]
e-mail: Sojka@ecn.purdue.edu

Maurice J. Zucrow Laboratories,
School of Mechanical Engineering,
Purdue University,
500 Allison Road,
West Lafayette, IN 47907-2014

The objective of this study was to develop an experimentally verified computational model that accurately predicts evolution of shear-thinning liquid jets. A secondary objective was to investigate the formation of satellite drops and to determine conditions under which their diameter can be controlled. The model employs the Galerkin finite/element approach to solve the complete two-dimensional set of axisymmetric governing equations and the corresponding kinematic and dynamic boundary conditions at the free surface. The effect of shear-thinning behavior on breakup was studied in detail for the case of an infinitely long non-Newtonian jet. It was found that shear-thinning behavior may be useful in controlling satellite drop sizes. (We observe that increasing the shear-thinning behavior at Re ~ 5 leads to an initial increase in the satellite drop size, followed by a subsequent decrease.) Comparison of model predictions with experimental data is presented for the case of a shear-thinning non-Newtonian jet. The experimental liquid was pumped through a capillary and drop shapes obtained using a high speed camera. The experimentally obtained shapes were compared to those predicted by the model and found to be in good agreement. [DOI: 10.1115/1.2956612]

1 Introduction

Drop formation in jets of non-Newtonian fluids is a commonly observed phenomenon. Applications in industry are widespread, viz., encapsulation processes for controlled drug delivery, inkjet printing, spray drying of starches, spray painting, and emulsification.

Liquid jet dynamics were first considered by Rayleigh [1] who examined the linear instability of an infinitely long viscous thread in an inviscid fluid. Linear and nonlinear analyses of Newtonian liquid thread breakup have been reviewed by Eggers [2]. In contrast, the analysis of viscoelastic liquid threads [3,4] and the breakup of purely viscous, shear-thinning, non-Newtonian liquid threads are still in its infancy. Yildirim and Basaran [5] analyzed the one- and two-dimensional breakup of a shear-thinning stretching bridge and showed that the difference between Newtonian and non-Newtonian bridges is significant for a large zero-shear viscosity, but insignificant for low zero-shear viscosity. They also noted that the evolution of a shear-thinning liquid bridge can be modeled as a Newtonian liquid bridge of lower viscosity, and that modifying the shear-thinning behavior might be useful in controlling or eliminating the formation of satellite drops. Finally, they reported discrepancies between results obtained from one- and two-dimensional analyses.

Doshi et al. [6] and Renardy and Renardy [7] proved the existence of self-similar solutions near pinch-off for power-law shear-thinning liquid threads, using a one-dimensional nonlinear analysis and a one-dimensional linear analysis in both the viscous and high inertia limits, respectively. They concluded that viscous and inertial forces were equally important near pinch-off.

To summarize, current literature has merely begun analyzing jets of shear-thinning non-Newtonian fluids. While similarity solutions explain the singularity of the jet at breakup, they are unable to predict drop sizes or drop shapes in shear-thinning jets.

To address this limitation we report the effect of power-law shear-thinning behavior for the case of a two-dimensional axisymmetric filament, at Re=5, by solving the entire Navier–Stokes equations. The arbitrary Lagrangian-Eulerian (ALE) Galerkin/finite element method, as described by Campana et al. [8], was employed to solve the ensuing system of nonlinear governing equations. We compare model predictions against experimental data obtained using jets of power-law non-Newtonian fluids exiting from capillary tubes. Drop formation from these capillary jets was captured using a high speed digital camera. Agreement is excellent.

2 Method of Approach

2.1 Governing Equations. Consider the deformation of an incompressible, shear-thinning, axisymmetric liquid filament of constant density ρ and zero-shear dynamic viscosity μ_0 surrounded by an inertialess gas. The cylindrical filament with uniform radius a is disturbed at time $t'=0$ by a sinusoidal wave with amplitude ε_0' and wavelength λ' (see Fig. 1). The position of the interface h' during instability evolution is considered to be a function of time t' and axial distance z'. Gravitational forces are neglected. The surface tension σ_0 on the filament interface is uniform.

Under these conditions, the mass and momentum balance in the filament are described by the dimensionless continuity and Navier–Stokes equations as follows:

$$\nabla \cdot \mathbf{v} = 0 \tag{1}$$

$$\mathrm{Re}\frac{D\mathbf{v}}{Dt} = \nabla \cdot \mathbf{T}, \quad \mathbf{T} = -p\mathbf{I} + \mu[\nabla\mathbf{v} + (\nabla\mathbf{v})^T] \tag{2}$$

where the following have been used: $(v_r, v_z) = (v_r', v_z')/(\sigma_0/\mu_0)$, $(r, z) = (r', z')/a$, and $p = ap'/\sigma_0$.

Since the length scale used is a and the velocity scale is σ_0/μ_0, the Reynolds number becomes $\mathrm{Re} = \rho a \sigma_0/\mu_0^2$.

The shear-thinning behavior is described by a three parameter Carreau model

[1]Present address: COMSOL, Inc., Waltham, MA 01803.
[2]Present address: Food Science Department, 745 Agriculture Mall Drive, West Lafayette, IN 47907.
[3]Corresponding author.

Contributed by the Fluids Engineering Division of ASME for publication in the JOURNAL OF FLUIDS ENGINEERING. Manuscript received May 31, 2007; final manuscript received April 16, 2008; published online July 29, 2008. Assoc. Editor: Dennis Siginer. Paper presented at the 2007 ASME International Mechanical Engineering Congress (IMECE2007), Seattle, WA, November 10–16, 2007.

 Copyright © 2008 by ASME

Downloaded From: https://fluidsengineering.asmedigitalcollection.asme.org on 06/30/2019 Terms of Use: http://www.asme.org/about-asme/terms-of-use

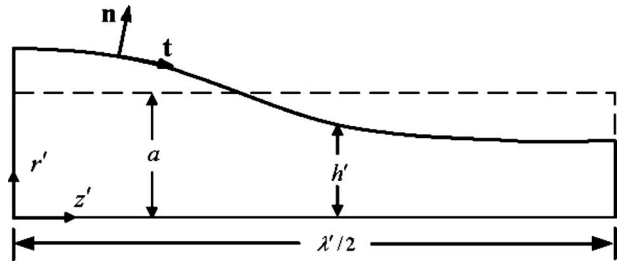

Fig. 1 System geometry with basic dimensions

$$\mu = (1-\beta)[1+(\alpha\dot{\gamma})^2]^{(n-1)/2} + \beta \tag{3}$$

where μ is the dimensionless apparent viscosity (also referred to as the effective viscosity) used in Eq. (2), α is a time constant, $0<\beta<1$ is the dimensionless infinite shear viscosity, n is the power-law index, and $\dot{\gamma}$ is the second invariant of the rate-of-deformation tensor. Neither elastic effects nor strain hardening is accounted for in the Carreau model.

Equations (1) and (2) were solved by imposing the symmetry boundary conditions and $\nabla\mathbf{v}\cdot\mathbf{n}=0$ at the centerline of the filament, plus $\mathbf{v}\cdot\mathbf{n}=0$ and $\partial h/\partial z=0$ at $z=0$ and $z=\lambda/2$, where $\mathbf{n}$ is the outward directed unit normal at the liquid phase free surface. On the filament interface, $r=h'(t,z)/a=h(t,z)$, and the conditions to be satisfied are the kinematic and dynamic boundary conditions.

At $t=0$, a sinusoidal spatial perturbation is applied to the gas-liquid interface

$$h(z,0) = 1 + \varepsilon_o \cos(kz) \tag{4}$$

where $\varepsilon_0=\varepsilon_0{}'/a$ is the amplitude of perturbation and $k=2\pi/\lambda$ is the dimensionless perturbation wave number.

2.2 Numerical Method. The set of two-dimensional nonlinear equations governing deformation of the liquid filament were solved using the Galerkin/finite element method for discretization in space and the finite difference method for discretization in time in order to obtain pressure and velocity fields and the location of the interface. We have previously applied essentially the same numerical procedure to study two-dimensional Faraday waves in Ref. [9]; it was discussed in detail there.

The jet was partitioned into a set of quadrilateral elements using the method of spines proposed by Kistler and Scriven [10]. Each element consists of two straight sides with fixed axial coordinates determined by spines parallel to the radial direction and of two curved sides that are determined by the deformation of the free surface. Following the standard finite element procedure [11], the four-node bilinear basis functions ψ^j used to weight the residual were also used to approximate the pressure field and the nine-node biquadratic finite element basis functions ϕ^j used to weight the residuals were also used to approximate the velocity field. On the interface, the nine-node biquadratic basis functions ϕ^j-collapse into one-dimensional biquadratic functions $\tilde{\phi}^j$, which were used to expand the shape of the interface.

The procedure described above reduces the set of governing partial differential equations to a system of nonlinear ordinary differential equations in time. To solve this system we follow the method described by Gresho et al. [12]. After discretization in time, the resulting system of nonlinear algebraic equations was solved using the Newton method at each time step. The time steps were adaptively chosen using the method of Crisfield [13].

3 Results and Discussion

3.1 Simulations. To ensure model accuracy, predictions were first compared with the one-dimensional nonlinear similarity solution near pinch-off for a power-law generalized Newtonian liquid jet, as computed by Doshi et al. [6]. This similarity solution has the form $\tau\sim h_{\min}^n$, where τ is the time to breakup, $h_{\min}$ is the minimum radius of the filament, and n is the power-law index. As Fig. 2 shows, agreement is within 0.1% for the region of $10^0 \geq \tau \geqslant 10^{-2}$.

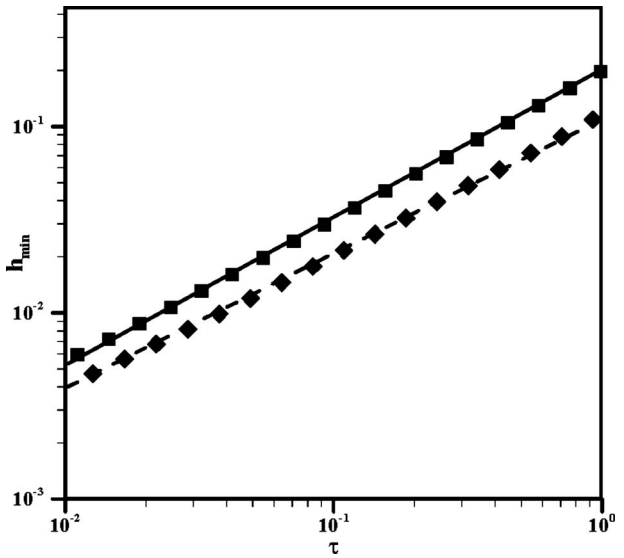

Fig. 2 Comparison of model predictions (symbols) with the similarity solution results of Doshi et al. [6] (solid line). Re=0, ε_0=0.5, α=1, β=0.02; n=0.8 (squares), n=0.9 (diamonds).

All computational results used an initial perturbation amplitude, ε_0, of 10^{-3}. When investigating the influence of non-Newtonian rheological behavior a dimensionless wave number, k, of 0.54 was chosen. This value was obtained from Timmermans and Lister [14] and corresponds to the maximum growth rate for a Newtonian fluid at Re=10.

All values for variables are reported in dimensionless form. The time to break up is defined as that at which the radius of the filament is reduced to, or falls below, 1/100 of the initial filament radius. This limit was chosen in order to avoid excessive distortion of the computational grid and to prevent numerical errors from entering the results.

We begin the discussion by examining the effect of the power-law index on drop formation at a moderate Reynolds numbers (Re=5), in particular, the formation of satellite drops. For the purposes of computation, we assume a single satellite drop is formed between two main drops and equate its diameter to that of a sphere whose volume lies between the two pinch-off points.

Figure 3 shows a steady increase in satellite drop radius as power-law index decreases from unity to 0.5. However, as n decreases below 0.5, satellite drop radius decreases slightly. This phenomenon has not been reported in scientific literature. To understand it, we first examine the transition to pinch-off for a Newtonian jet and compare it with the transition for a non-Newtonian jet.

As seen in Fig. 1, the initial perturbation imposed on the uniform jet causes a spatial difference in curvature along the jet. This difference in curvature results in a surface-tension driven pressure gradient. Figure 4(*a*) shows the flow streamlines in a Newtonian jet at $t=86.05$. The forces that act on the fluid are the inertial force, driving the fluid towards the main drop; the pressure gradient, also driving the fluid towards the main drop; and the viscous force, which opposes the flow. Here the entire flow is in the direction of the main drop, due to the initial condition imposed on the jet.

Bulk flow into the main drop is also observed in Fig. 5, which presents surface pressure and tangential velocity for the case corresponding to Fig. 4(*a*). Figure 5(*a*) shows that the pressure gradient is from the right to the left. Consequently, as shown in Fig.

Downloaded From: https://fluidsengineering.asmedigitalcollection.asme.org on 06/30/2019 Terms of Use: http://www.asme.org/about-asme/terms-of-use

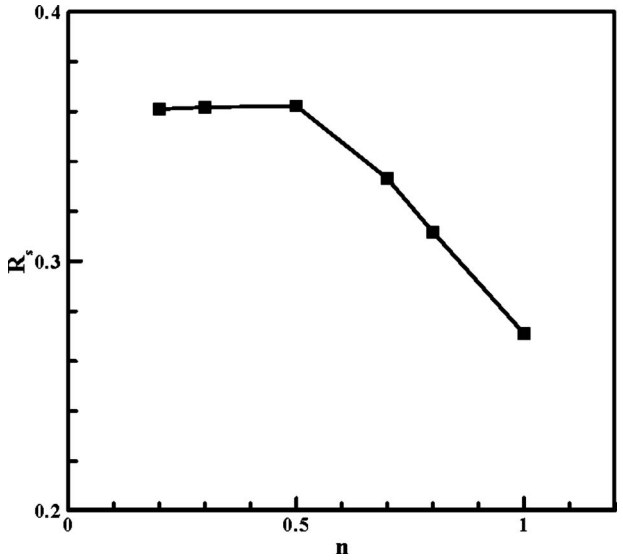

Fig. 3 Satellite drop radius versus power-law index *n* for Re =5, α=10, and β=0.002

5(*b*), the entire surface moves toward the main drop. This pressure gradient, in conjunction with the viscous force, finally reverses the flow from the main to the satellite drop, as seen in Fig. 4(*c*), which shows streamlines at t=92.0. This behavior is further illustrated in Fig. 6, which shows the surface pressure and surface tangential

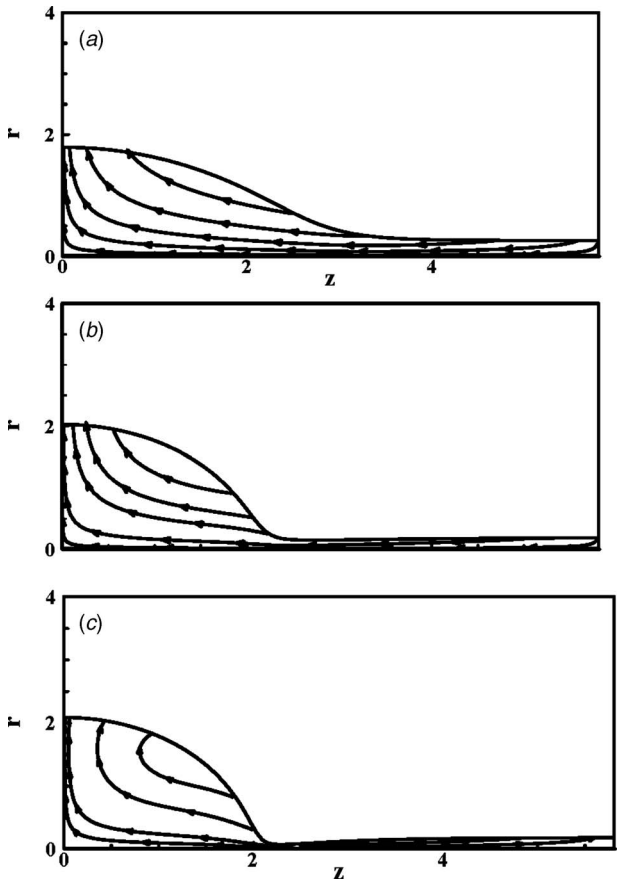

Fig. 4 Streamlines for a Newtonian jet with Re=5 at three dimensionless times before pinch-off: (*a*) t=86.05, (*b*) t=90.05, and (*c*) t=92.00.

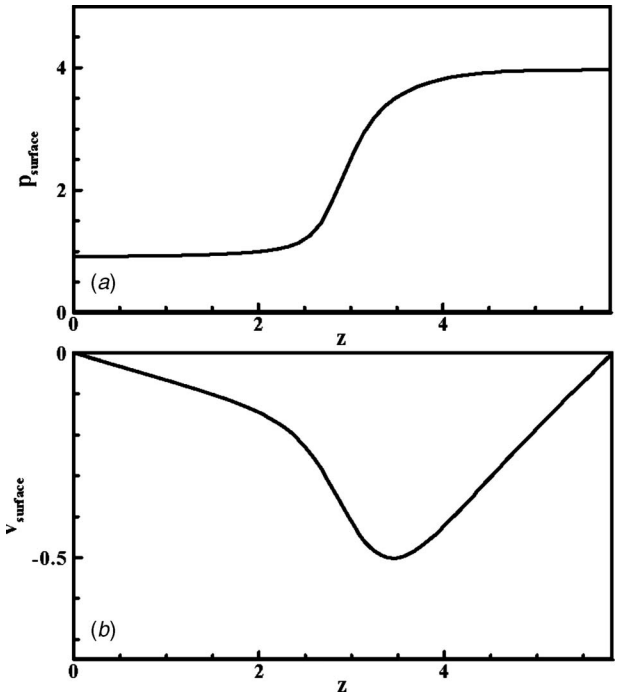

Fig. 5 Axial variation in the surface pressure (*a*) and surface tangential velocity (*b*) for a Newtonian jet of Re=5 at t=86.05

velocity at t=92.0. Figure 6(*a*) shows that there is a pressure gradient from the neck to the satellite drop. The change in direction of the velocity implies flow reversal.

Having understood the process of drop formation in a Newtonian jet, we now explain the effect of shear-thinning behavior on satellite drop formation at Re=5. Figure 7 demonstrates how the pinch-off and stagnation times (t_{stag} is defined as the time when the flow reverses into the satellite drop) change with variations in

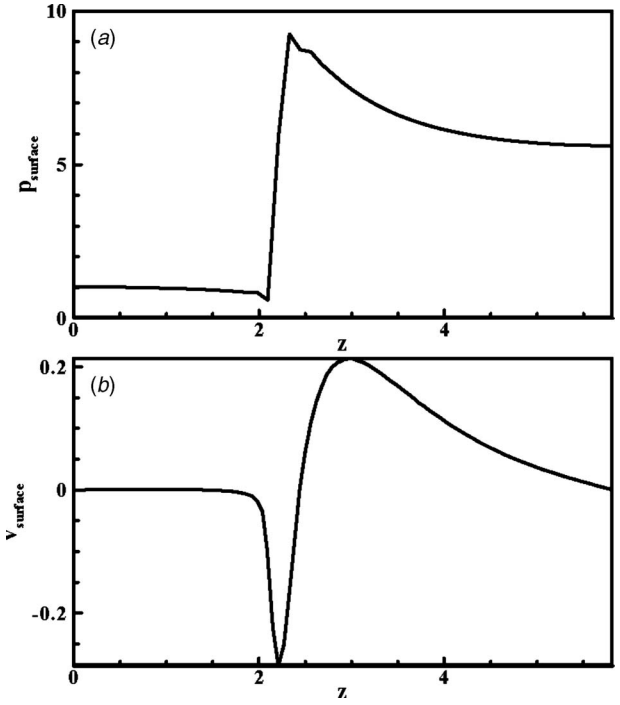

Fig. 6 Axial variation in the surface pressure (*a*) and tangential velocity (*b*) for a Newtonian jet of Re=5 at t=92.0

Downloaded From: https://fluidsengineering.asmedigitalcollection.asme.org on 06/30/2019 Terms of Use: http://www.asme.org/about-asme/terms-of-use

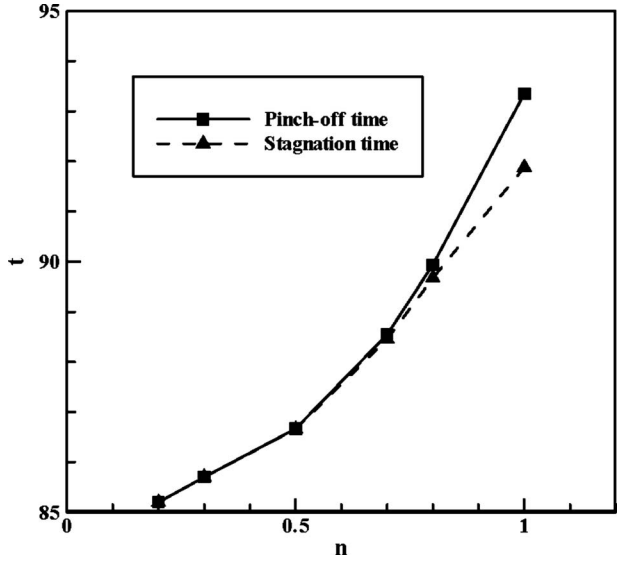

Fig. 7 Pinch-off time (solid line) and stagnation time (dashed line) versus power-law index for Re=5

the power-law index. Note that both the time to pinch-off and the stagnation time decrease as the power-law index decreases. However, the difference between the pinch-off and stagnation times decreases as the power-law index decreases, until eventually there is no reversal into the satellite drop. This is clearly illustrated by the streamlines in Fig. 8 ($n=0.3$). Figure 8(a) shows streamlines at $t=74.3$, which is before neck formation. At this time the entire flow moves toward the main drop, due to the imposed initial condition as explained previously. Figure 8(b) shows streamlines within the same jet at $t=85.5$, after the formation of a neck. At this instant, the entire flow moves towards the main drop despite neck formation.

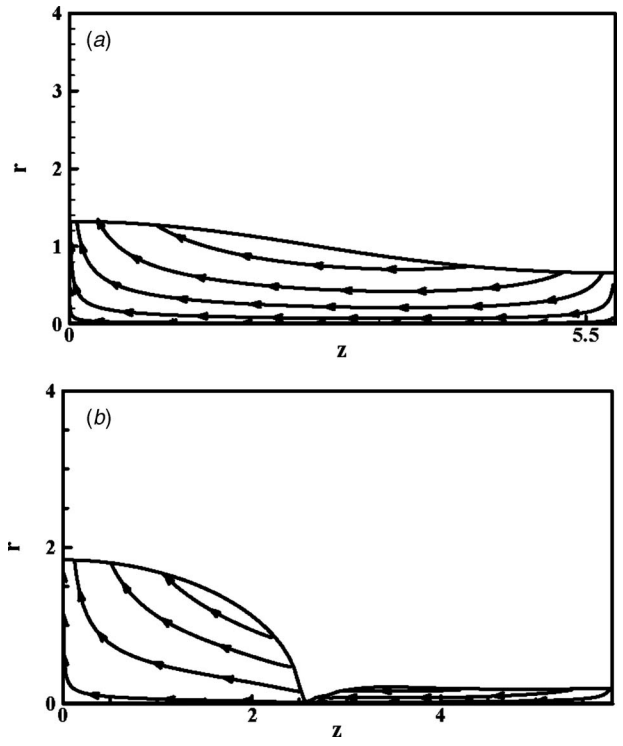

Fig. 8 Streamlines for a shear-thinning jet ($n=0.3$) at Re=5: (a) $t=74.3$ and (b) $t=85.5$

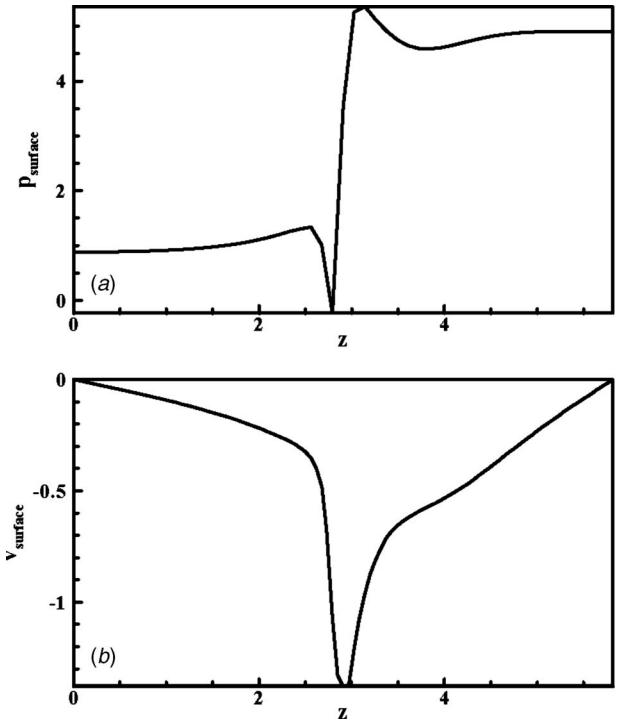

Fig. 9 Axial variation in the surface pressure (a) and surface tangential velocity (b) for $n=0.3$ and Re=5 at $t=85.5$

Figure 9 contains the surface pressure and tangential velocity for the non-Newtonian jet of Fig. 8(b), where there is a pressure gradient from the neck to the satellite drop. However, despite this gradient, the entire fluid moves toward the main drop, as can be seen from Fig. 8(b), which shows no change in direction of the surface tangential velocity. This behavior can be explained by two phenomena changes, which occur as a jet transitions from Newtonian to non-Newtonian. First, the normal pressure increases due to a decrease in the normal viscous forces. Second, the shear stresses opposing inertial flow towards the drop decrease due to a reduction in the effective viscosity.

Figure 10 shows the surface normal pressure at two different

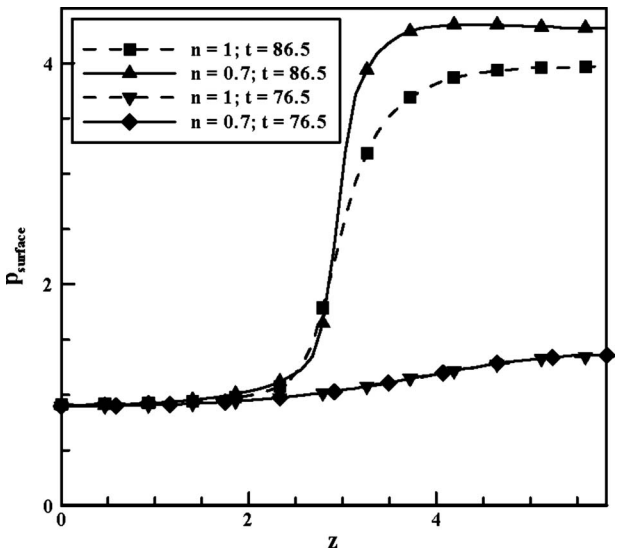

Fig. 10 Capillary pressure at the liquid interface for two times. The dashed line denotes a Newtonian jet and the solid lines denote a shear-thinning jet ($n=0.7$)

Downloaded From: https://fluidsengineering.asmedigitalcollection.asme.org on 06/30/2019 Terms of Use: http://www.asme.org/about-asme/terms-of-use

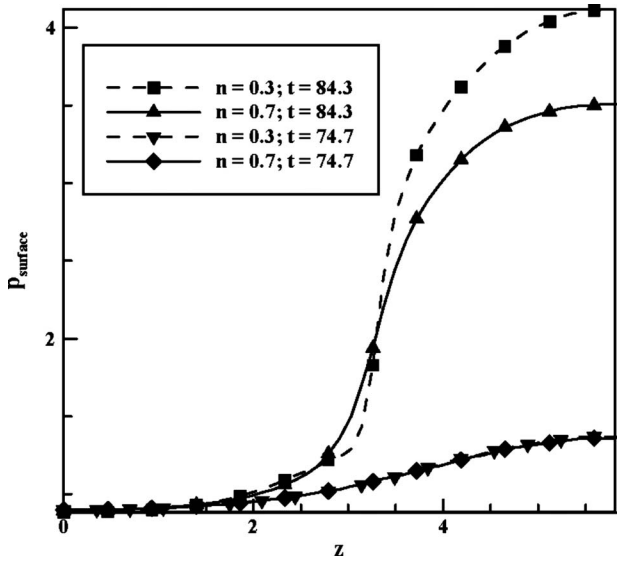

Fig. 11 Capillary pressure at the liquid interface for two times. Here the dashed line denotes a shear-thinning jet with $n=0.7$ while the solid line indicates a shear-thinning jet with $n=0.3$.

times for Newtonian and non-Newtonian jets. Initially, due to low shear rates, the surface normal pressure is similar for both cases. However, the shear rates in the non-Newtonian jet increase more rapidly as time progresses so at a later instant in time the normal surface pressure in a non-Newtonian jet is much higher than that in a Newtonian one.

It is also noted that the surface pressure is slightly lower at the right end of the domain than at the center for the shear-thinning jet. This is due to the onset of neck formation, whose curvature leads to a pressure gradient from the neck to the satellite. The increased normal pressure seen in Fig. 10 explains the earlier pinch-off times and earlier flow reversal times as the jet transitions from $n=1$ to $n=0.7$. The normal forces that lead to early reversal result in less fluid drainage into the main drop, which results in an increase in the satellite drop size as the power-law index is reduced.

Figure 11 shows the surface normal pressure at two different times for two different shear-thinning jets ($n=0.3$ and $n=0.7$). Here the surface pressure for a shear-thinning jet at $n=0.3$ is slightly higher than that for $n=0.7$, even at low shear rates. As the shear rates increase with time, the surface pressure in the jet with $n=0.3$ increases much more rapidly than for a jet with $n=0.7$. In addition, while the normal pressure increases, the reduction in effective viscosity fails to resist the initial flow towards the main drop before the normal forces cause pinch-off. This explains the lack of flow reversal at low power-law indices as seen in Fig. 7. This prevention of flow reversal, combined with earlier pinch-off times as the power-law index falls, leads to the absence of an increase in satellite drop size as the power-law index is reduced.

3.2 Comparison of Simulations and Experiments. Experiments to provide data for evaluating model accuracy were carried out with jets of power-law non-Newtonian fluids exiting from capillary tubes. Drop formation from these capillary jets was captured using a high speed digital camera. Digitized drop shapes were then compared to simulation results generated using the model described above.

The experimental apparatus included the following.

- A KD Scientific syringe pump with controllable flow rate that was used to force fluid through a Teflon® capillary tube (Upchurch Scientific®) with an inner diameter of 200 ± 20 μm. The axis of symmetry of the tube was aligned vertically.

Table 1 Physical properties for XG-water solutions

XG concentration (%)	n	μ_0 (mPa s)	σ (mN/m)	ρ (kg/m^3)
0.1	0.55	359 ± 9	72 ± 1	999 ± 1
0.2	0.40	732 ± 2	73 ± 1	999 ± 1
0.2	0.30	884 ± 1	73 ± 1	1000 ± 1

- A Phantom v7.1 high speed digital camera for visualization of the drop formation process. It can record images at 14,000 frames/s and has a pixel size of 14 μm. The camera was mated to a Nikon Nikkor™ lens with a focal length of 70 mm.
- A 200 W incandescent lamp for illumination of the experimental domain. The source was placed to provide backward lighting through a diffusive screen. Output from the camera was processed using NIH freeware.

The non-Newtonian liquids were Xanthan gum (XG) water solutions having concentrations of 0.1, 0.2, and 0.3% by weight. Their viscosities were measured using a Rhelogica Viscotech® rheometer. Power-law indices were determined by a fit to the shear stress and strain rate data (see Table 1). The confidence interval for the best-fit curves used to determine the power-law index was 95%.

When comparing experimental data and model simulations, Table 1 power-law index values were used along with a dimensionless infinite shear viscosity, β, of 0.002 and a time constant, α, of 10, as prescribed by Doshi et al. [6]. The values chosen (n ranging from 0.55 to 0.3) serve to validate the model predictions as all the analyses that have been performed were for $n\geqslant0.3$. Perturbation wave numbers were determined for each jet Re value from Timmermans and Lister's results [14].

Surface tensions were measured using a DuNuoy tensiometer, which had an accuracy of 0.001 N/m (CSC Scientific). Liquid densities were determined by weighing a known volume of the fluid on a Sartorius analytical balance (resolution 0.01 g). Liquid physical properties are summarized in Table 1. All experiments and physical property measurements were performed at $24.3\pm0.1\,^{\circ}$C.

Experimental operating conditions are listed in Table 2. Reynolds numbers were computed using initial liquid velocities determined from measured volumetric flow rates. The choice of Reynolds number range (0.19–0.65) is appropriate for assessing model accuracy since we have shown that shear-thinning behavior has the strongest effect on drop formation at low Re [15].

In passing, we note that that the Froude number (gd_c/u_0^2, where d_c is the dimensional diameter of the capillary and u_0 is the dimensional jet mean velocity) is $\sim10^{-5}$, while the Bond number ($\rho gr'^2/\gamma$) is $\sim10^{-4}$. These values provide support for our assumption that gravitational forces are negligible in comparison to surface-tension and inertial forces.

Based on the work of Gaster [16], who found that spatially

Table 2 Experimental operating conditions

XG concentration (%)	Reynolds number
0.1	0.46 ± 0.01
	0.55 ± 0.02
	0.67 ± 0.02
0.2	0.22 ± 0.01
	0.28 ± 0.02
	0.33 ± 0.02
0.3	0.19 ± 0.01
	0.23 ± 0.02
	0.28 ± 0.02

Downloaded From: https://fluidsengineering.asmedigitalcollection.asme.org on 06/30/2019 Terms of Use: http://www.asme.org/about-asme/terms-of-use

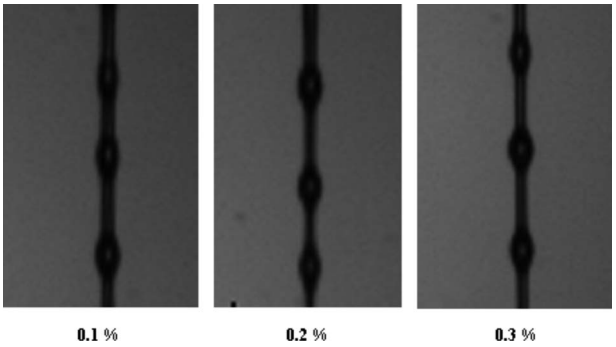

Fig. 12 Typical experimental droplet streams

increasing instability is negligible compared to temporally increasing instability for an infinitely long Newtonian liquid jet surrounded by an inviscid environment, we have assumed that the same holds true for shear-thinning jets. Therefore, drop shapes were captured at various times, with the time defined as $t' = d_n/v_0$, where d_n is the distance from the nozzle to the drop and v_0 is the initial liquid velocity. The experimental data collection times were arbitrarily chosen. Their magnitudes and uncertainties are included in the figure legends. Since each of the result figures is for jet breakup at a different time value, results were acquired throughout the breakup process thereby helping us to assess the accuracy of the model at all times up to pinch-off.

A typical screenshot is provided in Fig. 12. Individual droplet images were clipped from their corresponding total image, jet boundaries defined using a MATLAB routine, and then processed into black and white images (see Fig. 13). The image analysis routine then divided the droplet into two halves by imposing a centerline. The locations of the pixels at the left and right drop boundaries were determined for each image row, averaged and plotted for comparison with model predictions at the same time.

Uncertainty in the experimental results arises from (i) uncertainty in digitally processing the images and (ii) uncertainty in rheological data. For (i), the uncertainty $u_d/d = 1/N_p$ is defined by the smallest measurable unit (a pixel) where u_d is the uncertainty in the distance measured, d is the distance measured during image processing, and N_p is the number of pixels counted in an image. Uncertainties in the rheological data enter through the Reynolds number since it is an input to the model. This includes uncertainties in the liquid density and viscosity, in the jet diameter, and in the jet velocity. Density uncertainty includes contributions from the measured volume and mass. Viscosity uncertainty includes contributions from the measured torque and the sensor diameter. Velocity uncertainty includes contributions from the measured flow rate (volume and time) and the jet diameter. All were calculated using the approach of Kline and McClintock [17].

Comparisons of model predictions and experimental data are presented in Figs. 14 through 19 uncertainties. Model predictions are represented by solid lines, with their associated uncertainties indicated by dashed lines.

Figures 14 and 15 contain results for the highest and lowest Re cases when using the 0.1% XG-water solution. Model predictions

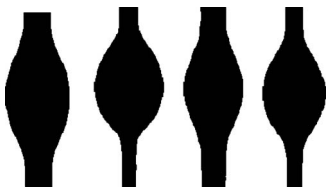

Fig. 13 Typical extracted images of postprocessed droplets

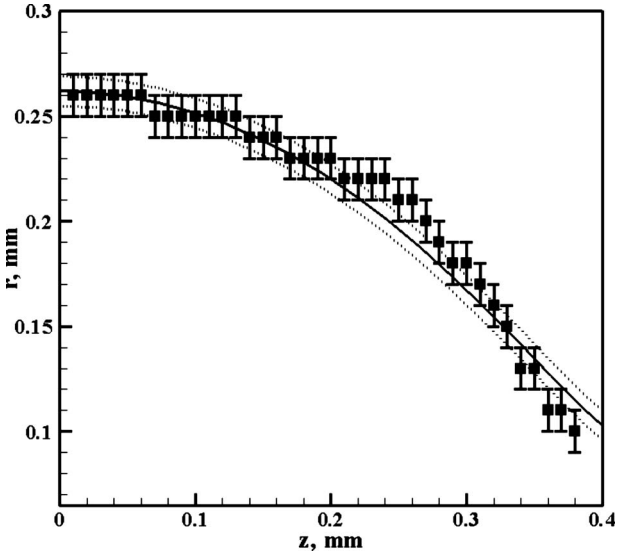

Fig. 14 Comparison of model predictions (solid line) with experimental data (square symbols) for 0.1% water-XG solution at Re=0.46, n=0.55, and t=9.61±0.09 ms. The dashed lines indicate the uncertainty in model predictions.

are equal to experimental data to within the sum of their uncertainties. Agreement is better for the higher Re case, especially nearest the pinch-off point.

Figures 16 and 17 contain results for highest and lowest Re cases when using the 0.2% XG-water solution. Model predictions are again equal to experimental data to within the sum of their uncertainties, and agreement is again better for the higher Re case, especially near pinch-off.

Figures 18 and 19 contain results for highest and lowest Re cases when using the 0.3% XG-water solution. As in the two previous cases, model predictions are equal to experimental data to within the sum of their uncertainties. Also, agreement is better for the higher Re case, especially nearest the pinch-off point.

In summary the data in Figs. 14–19 demonstrate that model predictions accurately match experimental data.

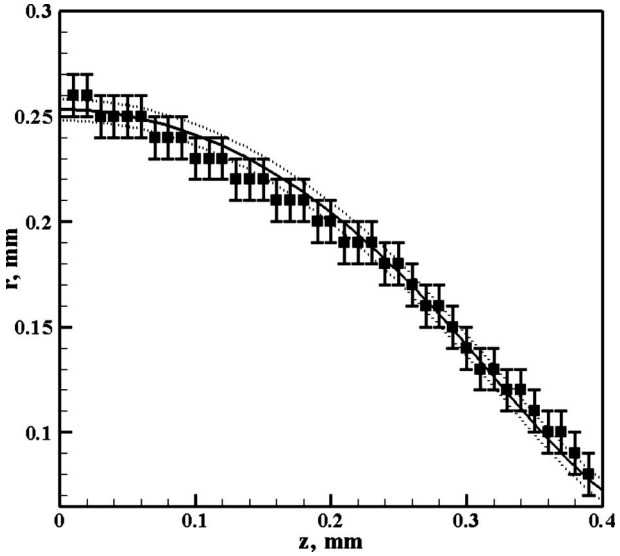

Fig. 15 Comparison of model predictions (solid line) with experimental data (square symbols) for 0.1% water-XG solution at Re=0.67, n=0.55, and t=9.09±0.08 ms. The dashed lines indicate the uncertainty in model predictions.

Downloaded From: https://fluidsengineering.asmedigitalcollection.asme.org on 06/30/2019 Terms of Use: http://www.asme.org/about-asme/terms-of-use

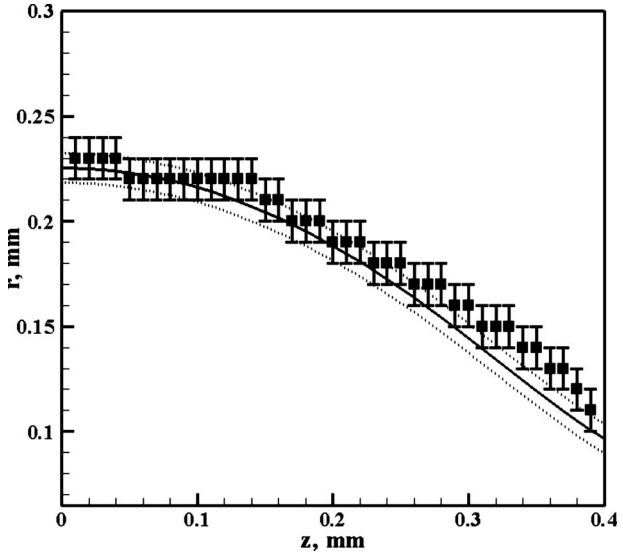

Fig. 16 Comparison of model predictions (solid line) with experimental data (squares) for 0.2% water-XG solution at Re =0.22, n=0.40, and t=12.48±0.05 ms. The dashed lines depict the uncertainty in model predictions.

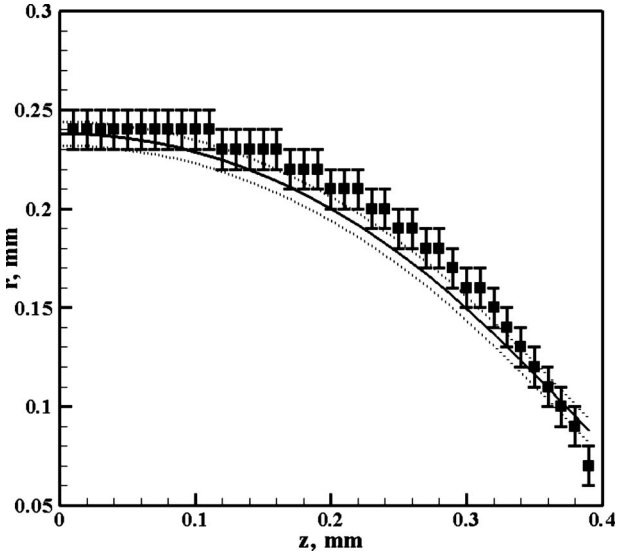

Fig. 18 Comparison of model predictions (solid line) with experimental data (square symbols) for 0.3% XG-water solution at Re=0.19, n=0.30, and t=12.80±0.09 ms. The dashed lines indicate the uncertainty in model predictions.

4 Summary and Conclusions

This study examined the effect of shear thinning on the behavior of a cylindrical jet. At Re=5, a decrease in the power-law index leads to an increase in satellite drop size. However, beyond a limiting power-law index, any further decrease leads to a slight decrease in the satellite drop size. This behavior is due to the twin effects of the increase in normal pressure and a reduction in viscosity as the power-law index falls. The increase in pressure leads to a reduction in pinch-off time, and also to earlier flow reversal as the power-law index is reduced. This lessens drainage into the main drop, which leads to an increase in the satellite drop diameter. Beyond a limiting power-law index there is no flow reversal into the satellite before pinch-off. This leads to the subsequent decrease in satellite drop size as the power-law index reduces further.

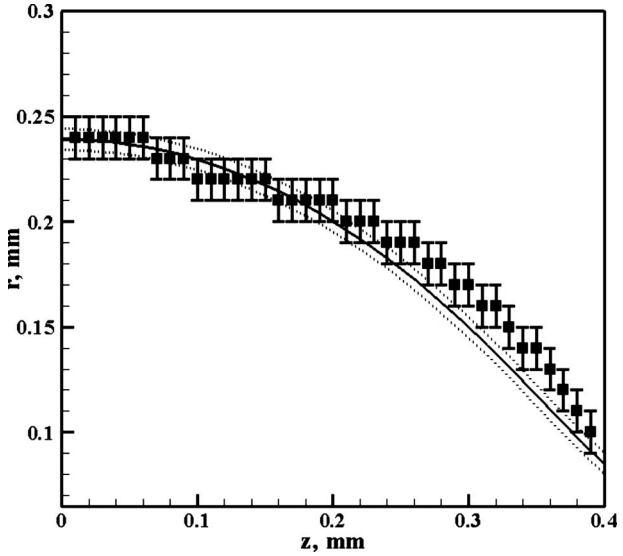

Fig. 17 Comparison of model predictions (solid line) with experimental data (square symbols) for 0.2% water-XG solution at Re=0.33, n=0.40, and t=10.88±0.07 ms. The dashed lines depict the uncertainty in model predictions.

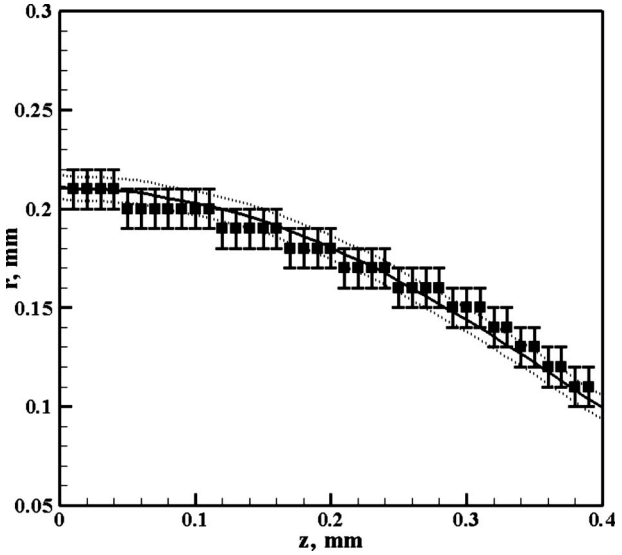

Fig. 19 Comparison of model predictions (solid line) with experimental data (square symbols) for 0.3% XG-water solution at Re=0.28, n=0.30, and t=10.63±0.08 ms. The dashed lines indicate the uncertainty in model predictions.

Model predictions were compared with experimental data. Agreement is within the sum of their uncertainties.

Acknowledgment

The authors gratefully acknowledge support from the National Science Foundation through Grant No. 323622-DMI.

References

[1] Rayleigh, L., 1879, "On the Instability of Jets," Proc. London Math. Soc., **10**, pp. 4–13.
[2] Eggers, J., 1997, "Nonlinear Dynamics and Breakup of Free-Surface Flows," Rev. Mod. Phys., **69**(3), pp. 865–930.
[3] Renardy, M., 2002, "Self-Similar Jet Breakup for a Generalized PTT Model," J. Non-Newtonian Fluid Mech., **103**(2–3), pp. 261–269.
[4] Bousfield, D. W., Keunings, R., and Marucci, G., 1986, "Nonlinear Analysis of

Downloaded From: https://fluidsengineering.asmedigitalcollection.asme.org on 06/30/2019 Terms of Use: http://www.asme.org/about-asme/terms-of-use

the Surface-Tension Driven Breakup of Viscoelastic Liquid Filaments," J. Non-Newtonian Fluid Mech., **21**(1), pp. 79–97.
[5] Yildirim, O. E., and Basaran, O. A., 1999, "Deformation and Breakup of Stretching Bridges of Newtonian and Sheer-Thinning Liquids: Comparison of One- and Two-Dimensional Models," Chem. Eng. Sci., **56**(1), pp. 211–233.
[6] Doshi, P., Suryo, R., Yildirim, O. E., McKinley, G. H., and Basaran, O. A., 2004, "Scaling in Pinch-Off of Generalized Newtonian Fluids," J. Non-Newtonian Fluid Mech., **113**(1), pp. 1–27.
[7] Renardy, M., and Renardy, Y., 2004, "Similarity Solutions for Breakup of Jets of Power Law Fluids," J. Non-Newtonian Fluid Mech., **122**(1–3), pp. 303–312.
[8] Campana, D., Paolo, J. D., and Saita, F. A., 2004, "A 2-D Model of Rayleigh Instability in Capillary Tubes Surfactant Effects," Int. J. Multiphase Flow, **30**, pp. 431–454.
[9] Ubal, S., Corvalan, C., Giavedoni, M. D., Saita, F. A., 2001, "A Numerical Study on Two-Dimensional Faraday Waves," *Computational Fluid and Solid Mechanics*, K. J. Bathe, ed., Springer New York, pp. 1000–1005.
[10] Kistler, S. F., and Scriven, L. E., 1983, *Coating Flows Computational Analysis of Polymer Processing*, J. R. A. Pearson and S. M. Richardson, ed., Applied Science, New York.
[11] Strang, G., and Fix, G. L., 1973, *An Analysis of the Finite Element Method*, Prentice-Hall, Englewood Cliffs, NJ.
[12] Gresho, P. M., Lee, R. L., and Sani, R. L., 1980, *Recent Advances in Numerical Methods in Fluids*, Pineridge, Swansea, UK, Vol. 1, Chap. 3.
[13] Crisfield, M. A., 1981, "A Fast Incremental-Iterative Solution Procedure That Handles Snap-Through," Comput. Struct., **13**(1–3), pp. 55–62.
[14] Timmermans, M.-L. E., and Lister, J. R., 2002, "The Effect of Surfactant on the Stability of a Liquid Thread," J. Fluid Mech., **459**, pp. 289–306.
[15] Dravid, V., Loke, P. B., Corvalan, C. M., and Sojka, P. E., 2006, "Drop Formation in Non-Newtonian Jets at Low Reynolds Numbers," *Proceedings of 2006 IMECE*, Chicago, IL, Nov.
[16] Gaster, M., 1962, "A Note on the Relation Between Temporally-Increasing and Spatially Increasing Disturbances in Hydrodynamic Stability," J. Fluid Mech., **14**, pp. 222–224.
[17] Kline, S. J., and McClintock, F. A., 1953, "Describing Uncertainties in Single Sample Experiments," Mech. Eng. (Am. Soc. Mech. Eng.), **75**, pp. 3–8.

Downloaded From: https://fluidsengineering.asmedigitalcollection.asme.org on 06/30/2019 Terms of Use: http://www.asme.org/about-asme/terms-of-use